International Journal of Impact Engineering 155 (2021) 103905

Contents lists available at ScienceDirect

International Journal of Impact Engineering

journal homepage: www.elsevier.com/locate/ijimpeng

Mechanical response of kerogen at high strain rates

Xiaohe Wang [a,b], Xianfu Huang [a,b], Mengni Gao [a,b], Ya-Pu Zhao [a,b,*]

[a] State Key Laboratory of Nonlinear Mechanics, Institute of Mechanics, Chinese Academy of Sciences, Beijing 100190, China
[b] School of Engineering Science, University of Chinese Academy of Sciences, Beijing 100049, China

ARTICLE INFO

Keywords:
Kerogen aggregate in shale
Strain rate
Compressible hyper-viscoelasticity
Constitutive model

ABSTRACT

As the main organic component of shale, the kerogen has a direct impact on the shale reservoirs. A molecular aggregate is used to study mechanical behaviour of kerogen, of which the molecular weight distribution is rational conforming to the Gaussian distribution. The mechanical response of kerogen is obtained with different strain rates by using molecular dynamics simulations. The results show that kerogen shows material hardening and fracture strain decrease with the strain rate. In the plastic range, we analyse the causes of stress oscillation at the microscopic level, and obtain the relationship between the stress oscillation and hydrogen bond. A compressible hyper-viscoelastic constitutive model of kerogen is established, which describes the mechanical behaviour of kerogen with different strain rates. Our research provides a valuable insight in the kerogen properties, and helps to understand the mechanical behaviour of shale reservoirs from a micro-perspective.

1. Introduction

Kerogen is the primordial material of oil/gas. It is the most widespread organic carbon in crust, the main component of organic matter in shale, and the vital storage medium of oil/gas, named by Crum Brown in 1906. Shale is one of the most complicated natural materials, in which kerogen is the major solid component of the organic matter. Nowadays, the shale oil/gas are extracted by hydraulic fracturing [1-3]. The fracturing fluid has different effects on the component of shale, resulting in the complex macroscopic mechanical behaviour of the reservoirs [4]. The main influencing factors of the mechanical behaviour of shale are the contents of quartz, carbonate and organic matter. For shales, the increases in carbonate and quartz contents lead to an increase in Young's modulus, while it decreases with the increase of organic matter content, clay content and porosity [11]. Kerogen is not only different from inorganic components in the chemical composition, but also different in mechanical properties [5]. Therefore, the properties and distribution of kerogen have great influence on reservoir physical properties, the formation of natural cracks and the crack propagation in hydraulic fracturing, and the oil and gas recovery [6].

The injection of high-pressure medium will bring loads with different strain rates. The effect of loading rate on the mechanical behaviour of shale is very valuable for hydraulic fracturing design and borehole stability. The research of mechanical behaviour of kerogen with different impact loads is also worthwhile for the in-situ retorting technology. The reason is that the in-situ retorting of oil shale needs to destroy rock by explosion load. As the existence of kerogen greatly changes the characteristics of rock, the study of kerogen mechanical behaviour with different impact loads is an important part in mining [7]. But the current research rarely considers the effect of loading rate on the properties of kerogen [8]. Therefore, the study of mechanical properties of kerogen is very significant in Shale oil and gas exploitation.

The moduli of kerogen and quartz were obtained through the dynamic mapping technology of nano-indentation [9, 10]. And the distribution of shale components and Young's modulus of organic matter were also detected by the scanning electron microscopy (SEM) and the atomic force microscopy (AFM) [11]. The Young's modulus of kerogen measured by the nano-indentation is 1−15 GPa [9, 12, 13], and is 7−18 GPa by AFM [11, 14-16]. The content of organic carbon affects the micro seismic and acoustic wave velocities in shale. The existence of kerogen greatly changes the creep and fracture characteristics of shale [17, 18]. The strain softening of kerogen might skew the results in faster fracture closure when kerogen in the kerogen-rich micro-cantilever beam tension is in stretched state [19, 20]. Kerogen is an extremely complex organic matter composed of amorphous carbon skeleton [21-23], which is the softer components in shale and might be the fracture initiation point [5]. The mechanical properties of kerogen are closely related with its chemistry composition. The increase of the sp2/sp3 hybridization ratio of kerogen leads to an overlap from the ductile to brittle rupture mechanisms [24]. In addition, micropores are formed during kerogen

* Corresponding author.
E-mail address: yzhao@imech.ac.cn (Y.-P. Zhao).

https://doi.org/10.1016/j.ijimpeng.2021.103905
Received 8 January 2021; Received in revised form 26 April 2021; Accepted 28 April 2021
Available online 11 May 2021

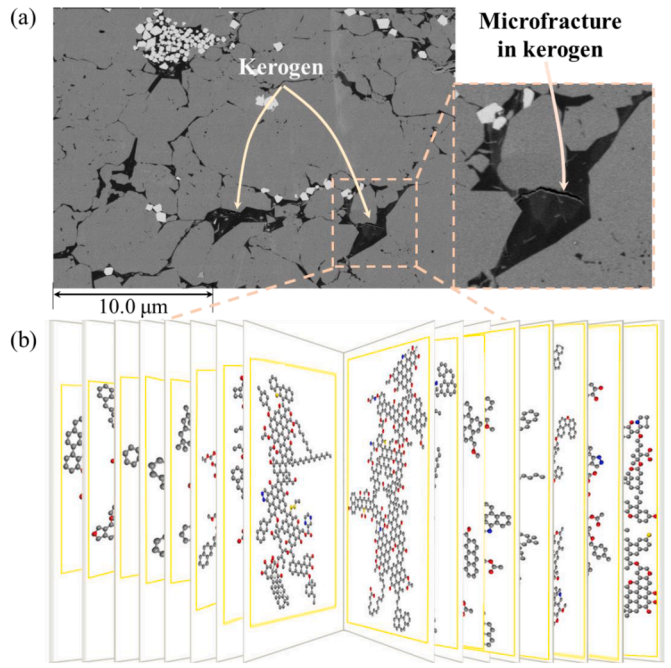

Fig. 1. Kerogen for MD simulations, (a) The SEM of shale, (b) Established kerogen molecular group. Kerogen carbon skeleton from C_{100}–C_{800}.

decomposition into gas and oil, and micro-fractures are generated due to the crustal stress and pore pressure [25-27]. This makes the asymptotic failure of kerogen caused by micro-fractures to be possible [28] The research on the mechanical properties of kerogen is mainly based on nano-indentation and AFM to study the moduli of kerogen. However, it is difficult to obtain the dynamic mechanical response of kerogen under loading.

The mechanical behaviour of kerogen can be estimated by the molecular dynamics (MD) simulation during the loading process based on the constructed kerogen model [5]. However, traditional MD simulation cannot be obtained the breakage/formation of chemical bonds, so the change of chemical bonds during deformation is missing in the study of mechanical properties of materials using MD simulations. As an alternative method, the reactive force field MD (Reaxff-MD) can simulate the bonds formation and breaking, which can be performed to study the mechanical behaviour of kerogen. For example, the elastic response of crosslinked epoxy has been generated by Reaxff-MD. The method was proved to be valuable for the prediction of yield point [29]. And the fracture mechanism of the calcium sulfate column during stretching was explained at the atomic scale by observing the breaking process of chemical bonds [30]. Reaxff-MD has been used in the mechanical study of graphene, metal systems, and polymers. The elastic modulus and fracture characteristics were obtained [31-33]. For polymer, the tensile moduli simulated by MD with Compass and Dreiding force field were much higher than those obtained by experiments, while the results of Reaxff-MD had very good correlation with those of experiments [34-36]. To ensure the accuracy of results of the simulations, the structural model of kerogen should be reasonable. However, the structures of kerogen were mostly built by one type of kerogen molecules, resulting in an irrational molecular weight distribution [5, 37, 38].

In this study, a large-scale kerogen molecular aggregate is established, which contains the structure information from experiments. The molecules of the aggregate are with a molecular weight conforming to the Gaussian distribution. The dynamic response of kerogen with different strain rates is obtained by Reaxff-MD simulations. And we observe the relation between the mechanical behaviour and atomic scale structural changes. Then the nonlinear elasticity of kerogen is described by the established compressible hyper-viscoelastic constitutive model.

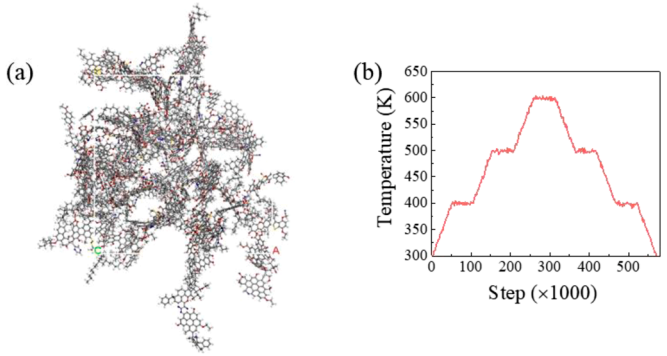

Fig. 2. Information of (a) the structure of kerogen aggregate (b) temperature of the model relaxation for (a).

The results provide a model basis for understanding the mechanical behaviour of shale as a complex medium.

2. Material and methods

2.1. Molecular group preparation

Kerogen was extracted from the shale sample which was taken from 2650 m underground in the Ordos basin as shown in Fig. 1(a). Kerogen was scattered in the shale, in which microfractures could be observed. Based on kerogen macromolecules model that we constructed before [39], a molecular group was established (Fig. 1(b)). 16 molecules were contained, of which the molecular weight is the Gaussian distribution. The information to construct those molecules was obtained by a series of experiments [40].The average molecular weight is about 5000 g/mol, which is consistent with the experimental results. [40, 41] The total carbon atom number is 5061, which means the molecular group is a large-scale model for kerogen. The structure contains reasonable chemical bonds, pyrolysis products and non-degradable experimental information. Compared to kerogen aggregates composed of just one type molecules, this structure is more reasonable to study its mechanical properties.

2.2. Kerogen aggregate by MD simulations

Kerogen macromolecules were optimized by molecular mechanics and annealing algorithm to eliminate the unreasonable bond and obtain the structures with the minimized global energy. The specific optimization steps were shown in the previous work [39]. Then, the macromolecules were placed in a lattice to minimize the energy of the entire molecular group. The annealing algorithm was performed again. The initial configuration of kerogen aggregates is shown in Fig. 2(a). Next, Reaxff-MD was used to conduct kerogen compression. The group was compressed to a structure with 1.13 g/cm^3 density through the isothermal-isobaric (NPT) ensemble, of which the density is similar to the experimental results [42]. The structure was relaxed by simulations of the canonical (NVT) and NPT ensemble to eliminate the local heterogeneities. As shown in Fig. 2(b), we used NVT ensemble for the heating and cooling process, while the NPT ensemble was employed for thermostatic steps. The time step was 0.25 fs. At last, we used the NPT ensemble at 300 K. The pressure was 0 MPa, and the simulation time was 1 ns to eliminate the residual stress in the structure. We can find that the volume occupied by macropores is reduced after the annealing algorithm (the probe sphere radius $>$ 2.8 Å). That means chemical chain is more relaxed in the structure, occupying the free volume in the initial model, and the density distribution is more uniform. The final density of kerogen was 1.14 g/cm^3. We chose the CHONSSi-lg.ff as the basic force field, which includes the long-range-correction terms [43]. But it cannot describe the interaction between S and O atoms well. Thus, we modify

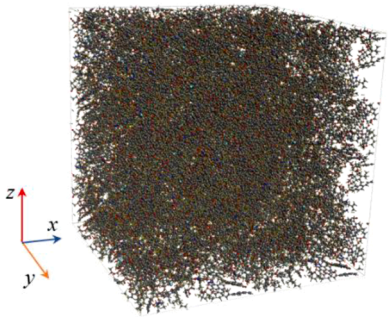

Fig. 3. The final configuration of kerogen aggregate.

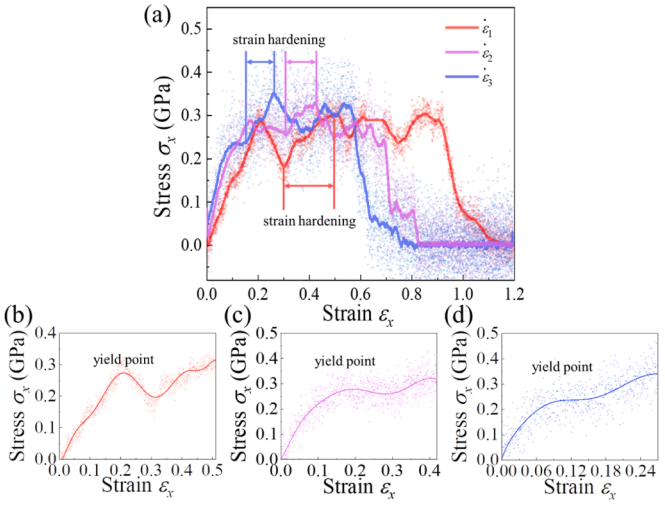

Fig. 4. Mechanical behaviour of kerogen under different strain rates by MD simulations. (a) The total stress-strain curves. The smooth curves of data points are obtained by adjacent average method. The simulation times are 0.84 ns, 0.46 ns and 0.23 ns with the strain rate $\dot{\varepsilon}_1$, $\dot{\varepsilon}_2$, and $\dot{\varepsilon}_3$, respectively (red points, purple points, and blue points, the fracture occurrs). The local curve including strain hardening stage under (b) $\dot{\varepsilon}_1$, (c) $\dot{\varepsilon}_2$ and (d) $\dot{\varepsilon}_3$. The curves of (b)–(d) are obtained by the polynomial fitting to characterize the trend of strain.

the SO function parameter to make it suitable for our structure (CHONS-lg). The structure was fully relaxed to eliminate unreasonable structure. The potential function of Reaxff-MD is

$$E = E_{\text{bond}} + \underbrace{E_{\text{over}} + E_{\text{under}}}_{\text{atomover-/under-coordination}} + \underbrace{E_{\text{val}} + E_{\text{pen}} + E_{\text{coa}}}_{\text{valenceangleterms}} + E_{\text{tors}} + \underbrace{E_{\text{C2}} + E_{\text{trip}} + E_{\text{conj}} + E_{\text{Hbond}} + E_{\text{lp}}}_{\text{specific}} + \underbrace{E_{\text{vdW}} + E_{\text{Coulomb}}}_{\text{non-bondedenergy}} \quad (1)$$

where E_{bond} is the bond energy, $E_{\text{over}}/E_{\text{under}}$ are the penalty energies for the over-/under-coordinated atoms, E_{val}, E_{pen}, and E_{coa} are the valence angle energy, the penalty energy for handling atoms with two double bonds, and the coalition (three-body conjugation) energy, E_{tors} is the torsion angle energy, E_{C2}, E_{trip}, E_{conj}, E_{Hbond}, and E_{lp} are the C2 correction, the triple bond energy correction, the four body conjugation term, the hydrogen bond energy, and the lone-pairs bond energy,E_{vdw} and E_{Coulomb} are the nonbonded van der Waals interactions energy and Coulomb interaction energy, respectively. The van der Waals interaction is the Morse-potential [43].

2.3. The uniaxial stretching by MD simulations

The volume of kerogen was 4.8 × 5 × 4.8 nm in Fig. 3. The stretching simulations were with periodic boundary condition using Reaxff-MD. The CHONS-lg was chosen as the force field. The Young's moduli obtained by Reaxff-MD are accurate enough comparing with the experimental results [34], so it can be used to study mechanical properties. The temperature, time and method were 300 K, 2 ns and NPT Berendsen, respectively. The lattice was stretched in the x direction. The deformations per step are fixed. The changes of each step of simulations were set as 1.19×10^{-6} nm, 5.94×10^{-6} nm, and 1.19×10^{-5} nm, of which the three strain rates were $\dot{\varepsilon}_1$, $\dot{\varepsilon}_2$ and $\dot{\varepsilon}_3$, respectively ($\dot{\varepsilon}_1 = 1 \times 10^8 s^{-1}$, $\dot{\varepsilon}_2 = 5 \times 10^8 s^{-1}$, $\dot{\varepsilon}_3 = 1 \times 10^9 s^{-1}$ at the beginning of deformation). The size changes with free boundaries in the y and z directions.

3. Results and discussion

3.1. Mechanical behaviour of kerogen aggregate

As an organic polymer, kerogen is the soft part in shale, which may be the initiation point of hydraulic fracturing and natural fractures. Fig. 1(a) shows a microfracture in kerogen. The mechanical responses of kerogen under different strain rates are obtained in Fig. 4. The stress-strain curves of kerogen deviate from the linear relationship before the yielding point. The local softening is related to the appearance of microfracture. And intermolecular interactions are disrupted, such as the H bond and π-π interaction broken. the After the yielding point, the strain hardening appears. The greater the strain rate is, the more obvious strain hardening effect is, and larger the ultimate strength is. Then, the stress fluctuates with the increasing strain, but the stress does not have a trend-change with the strain until fracture. The yield strengths, ultimate strengths, and fracture stresses, yield strains, and fracture strains were listed in Table 1 under three strain rates. With the increase of strain rate, the strains of kerogen at yield point and fracture point decrease.

The process of kerogen stretching with the strain rate $\dot{\varepsilon}_2$ is studied, as shown in Fig. 5(a). Kerogen molecules contain aromatic clusters that are the rigid part (compared to the long aliphatic chain). Micropores exist in kerogen, which lead to a not completely uniform structure, even if the unreasonable density part of the structure is eliminated by relaxation. The slippage between molecules and breaking of hydrogen bonds (H bonds) are likely to occur near a micropore. The micropore volume increases with stretching on the fracture surface. And there is a small amount of chemical bond changes during the stretching, which can be obtained by Reaxff-MD. The fracture is mainly composed of the intermolecular slippage with the breaking of the H bond. There are a large number of π bonds in type III kerogen. Due to the π-π interaction, the aromatic cluster is arranged mainly in parallel-stacking and a small part in the edge-to-face stacking. Near the fracture plane, the plane of aromatic ring is parallel to the stretching direction, and the aliphatic chains are straightened along the stretching direction. When the fracture occurs, the π-π interaction is broken. As shown in Fig. 5(b), H bonds are formed and broken during the stretching. After the fracture occurs, the straight long chain is back to curl state and aromatic ring returns to the

Table 1
The mechanical parameters of kerogen under different strain rates.

	The yield point			The ultimate strength			The fracture		
	$\dot{\varepsilon}_1$	$\dot{\varepsilon}_2$	$\dot{\varepsilon}_3$	$\dot{\varepsilon}_1$	$\dot{\varepsilon}_2$	$\dot{\varepsilon}_3$	$\dot{\varepsilon}_1$	$\dot{\varepsilon}_2$	$\dot{\varepsilon}_3$
Stress σ_x (GPa)	0.29	0.29	0.24	0.30	0.32	0.35	0.29–0	0.24–0	0.31–0
Strain ε_x	0.21	0.17	0.12	–	0.42	0.26	0.90–1.13	0.70–0.85	0.56–0.76

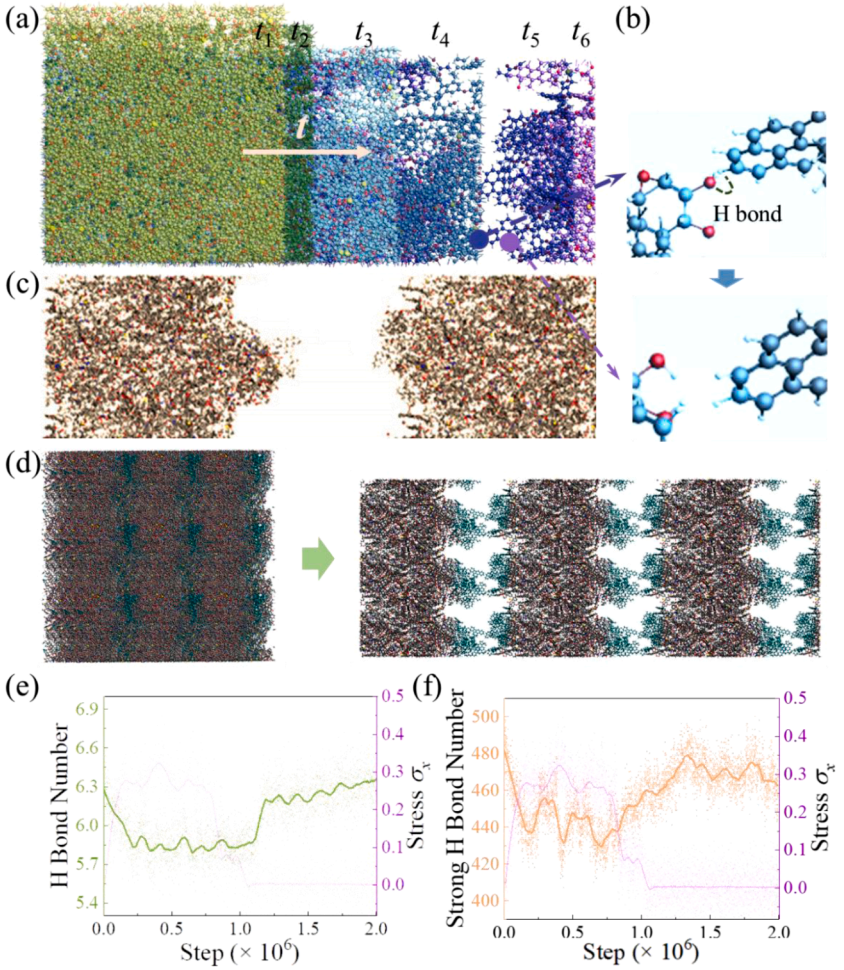

Fig. 5. The analysis of kerogen mechanical behaviour, (a) deformation process of kerogen, (b) H bond breaking on the fracture surface, (c) the microfracture of kerogen, (d) the fracture plane of kerogen aggregate. The bright green part are the atoms at the fracture surface. The periodic cells are shown to exhibit the fracture surface (3 × 3 × 3). (e) The number of H bond (× 10^3) versus stress, (f) the strong H bond number versus stress. The simulation time is 0.5 ns with a strain rate of $\dot{\varepsilon}_2 = 5 \times 10^8 s^{-1}$, with an engineering strain of 1.25 (part of the 2 ns).

parallel stacking. Microfracture forms during stretching as shown in Fig. 5(c) and (d). The oscillation behaviour of kerogen is closely related to the H bonds. In the elastic phase, as the strain increases, the number of H bonds decreases. In the plastic range, the stress oscillation appears. We think that this phenomenon is related to the breaking and formation of H bonds. The results in Fig. 5(e) and (f) show that the oscillation trend of the number of H bonds is very similar to that of stress. Strain hardening occurs as the number of strong H bond increases. As the number of H bonds decreases, the stress drops because some H bonds are broken during the stretching process. Thus, part of the long chain and aromatic structure return to equilibrium from the stretched state, during which time stress is relieved. As the stress is released, part of the structure shrinks, and new H bonds are formed. Therefore, the strain hardening occurs. The phenomenon is called as a stress oscillation event.

3.2. Basic theory

In order to study the deformation of kerogen, the reference configuration and the current configuration are represented by $\boldsymbol{X}$ and $\boldsymbol{x}$, respectively [44]. φ is the functional relationship between the $\boldsymbol{x}$ and $\boldsymbol{X}$. Then, we have

$$\mathrm{d}\boldsymbol{x} = \varphi(\boldsymbol{X} + \mathrm{d}\boldsymbol{X}, t) - \varphi(\boldsymbol{X}, t) = \boldsymbol{F}\mathrm{d}\boldsymbol{X} \tag{2}$$

where $\boldsymbol{F}$ is the deformation gradient tensor as $\boldsymbol{F} = \frac{\mathrm{d}\boldsymbol{x}}{\mathrm{d}\boldsymbol{X}} = \frac{\partial x_i}{\partial X_K}\boldsymbol{e}_i \otimes \boldsymbol{e}_K$.

The Green strain tensor is defined as [44]

$$\boldsymbol{E} = \frac{1}{2}\left(\boldsymbol{F}^{\mathrm{T}}\boldsymbol{F} - \mathbf{I}\right) \tag{3}$$

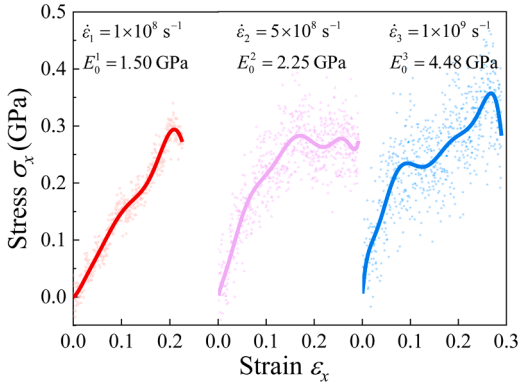

Fig. 6. The stress-strain relationship of kerogen exhibiting small deformation (the smooth curves obtained by adjacent average method).

The right Cauchy-Green deformation tensor is $\boldsymbol{C} = \boldsymbol{F}^{\mathrm{T}}\boldsymbol{F}$. The principal invariants of $\boldsymbol{C}$ are

$$\begin{cases} \mathrm{I}_1 = \mathrm{tr}\boldsymbol{C} = 3 + 2\mathrm{tr}\boldsymbol{E} \\ \mathrm{I}_2 = \frac{1}{2}\left(\mathrm{tr}^2\boldsymbol{C} - \mathrm{tr}\boldsymbol{C}^2\right) \\ \mathrm{I}_3 = \det\boldsymbol{C} \end{cases} \tag{4}$$

The Piola-Kirchhoff 2 (PK2) stress is expressed by the strain energy function w as

$$\boldsymbol{T}=\frac{\partial w}{\partial \boldsymbol{E}}=\frac{\partial w}{\partial \mathrm{I}_1}\frac{\partial \mathrm{I}_1}{\partial \boldsymbol{E}}+\frac{\partial w}{\partial \mathrm{I}_2}\frac{\partial \mathrm{I}_2}{\partial \boldsymbol{E}}+\frac{\partial w}{\partial J}\frac{\partial J}{\partial \boldsymbol{E}} \tag{5}$$

where $\frac{\partial \mathrm{I}_1}{\partial \boldsymbol{E}}=2\mathbf{I}$, $\frac{\partial \mathrm{I}_2}{\partial \boldsymbol{E}}=2(\mathrm{I}_1\mathbf{I}-\boldsymbol{C})$, and $\frac{\partial J}{\partial \boldsymbol{E}}=J\boldsymbol{C}^{-1}$.

3.3. The compressible hyper-elastic equation for kerogen

The Young's moduli of kerogen are calculated at the beginning of loading, as shown in Fig. 6. The initial moduli are 1.50 GPa, 2.25 GPa and 4.48 GPa, which increase significantly with the strain rate. Kerogen shows the material hardening with the strain rate increasing and exhibits nonlinear mechanical behaviour. According to the properties of polymers, we consider the hyper-elasticity and viscoelasticity of kerogen.

As shown in the Fig. 6, kerogen is with the nonlinear stress-strain relationship, which is also affected by the strain rate. We consider that kerogen is mainly composed of aromatic clusters and aliphatic long chains. The chains are highly malleable exhibiting hyper-elasticity. In addition, kerogen also shows the phenomenon of stress relaxation. Hence, the hyper-viscoelastic constitutive model should be established.

Hyper-elastic models can be divided into phenomenological model and molecular chain network model. Phenomenological model includes the Ogden model, Mooney-Rivlin model, Yeoh model, etc. [45, 46] Molecular chain network model includes the Neo-Hookean model based on Gaussian chain and eight-chain non-Gaussian model and so on [47]. As a significant increase of volume during stretching of kerogen can be observed, a compressible hyper-elastic model should be established. Decomposing the deformation gradient tensor by multiplication, we obtain [48]

$$\boldsymbol{F}=\frac{\partial \boldsymbol{x}}{\partial \boldsymbol{p}}\frac{\partial \boldsymbol{p}}{\partial \boldsymbol{X}}=\boldsymbol{F}^{\mathrm{e}}\boldsymbol{F}^{\mathrm{s}} \tag{6}$$

where $\boldsymbol{p}$ is intermediate configuration, $\boldsymbol{F}^{\mathrm{e}}$ is the volume preserving the deformation gradient, and $\boldsymbol{F}^{\mathrm{s}}$ is the deformation gradient of bulging part.

For the three-dimensional problem, the Jacobian of $\boldsymbol{F}^{\mathrm{e}}$ can be calculated as $J_{\mathrm{e}}=\det\boldsymbol{F}^{\mathrm{e}}=1$, while the total Jacobian is

$$J=\det\boldsymbol{F}=\det(\boldsymbol{F}^{\mathrm{e}}\boldsymbol{F}^{\mathrm{s}})=\det\left(\boldsymbol{F}^{\mathrm{e}}J_{\mathrm{s}}^{1/3}\mathbf{I}\right)=\left(J_{\mathrm{s}}^{1/3}\right)^3\det\boldsymbol{F}^{\mathrm{e}}=J_{\mathrm{s}} \tag{7}$$

For the isotropic material, the deformation gradient of bulging part

$$\boldsymbol{F}^{\mathrm{s}}=J_{\mathrm{s}}^{1/3}\mathbf{I}=J^{1/3}\mathbf{I} \tag{8}$$

Then $\boldsymbol{F}^{\mathrm{e}}=\overline{\boldsymbol{F}}$, $\boldsymbol{F}=\boldsymbol{F}^{\mathrm{e}}\boldsymbol{F}^{\mathrm{s}}=J^{1/3}\overline{\boldsymbol{F}}$.

Among the hyper-elastic constitutive models, the Mooney-Rivlin model is a commonly used model suitable for small and medium deformations, and its strain energy function is [47]

$$w=c_{01}\left(\bar{\mathrm{I}}_1-3\right)+c_{10}\left(\bar{\mathrm{I}}_2-3\right)+D_1(J-1)^2 \tag{9}$$

where $\bar{\mathrm{I}}_1$, $\bar{\mathrm{I}}_2$ are the first invariant and second invariant of isochoric part $\overline{\boldsymbol{C}}$. c_{01}, c_{10} and D_1 are the material constants. The $D_1(J-1)$ is the strain energy of the bulging part. The invariants of $\overline{\boldsymbol{C}}$ they can be expressed by that of $\boldsymbol{C}$ and the principle stretch λ_i as

$$\begin{cases}\bar{\mathrm{I}}_1\left(\overline{\boldsymbol{C}}\right)=\bar{\mathrm{I}}_1\left(J^{-\frac{2}{3}}\boldsymbol{C}\right)=J^{-\frac{2}{3}}\mathrm{I}_1=J^{-\frac{2}{3}}\left(\lambda_1^2+\lambda_2^2+\lambda_3^2\right)\\ \bar{\mathrm{I}}_2\left(\overline{\boldsymbol{C}}\right)=\frac{1}{2}J^{-\frac{4}{3}}\left(\mathrm{tr}^2\boldsymbol{C}-\mathrm{tr}\boldsymbol{C}^2\right)=J^{-\frac{4}{3}}\mathrm{I}_2=J^{-\frac{4}{3}}\left(\lambda_1^2\lambda_2^2+\lambda_2^2\lambda_3^2+\lambda_3^2\lambda_1^2\right)\\ J=\det\boldsymbol{F}=\lambda_1\lambda_2\lambda_3\end{cases} \tag{10}$$

By substituting Eq. (10) into the Eq. (9), it can be expressed as:

$$w=c_{01}\left(J^{-2/3}\mathrm{I}_1-3\right)+c_{10}\left(J^{-4/3}\mathrm{I}_2-3\right)+D_1(J-1)^2 \tag{11}$$

Then the PK2 stress can be written as

$$\begin{aligned}\boldsymbol{T}&=\left(2J^{-2/3}c_{01}+2J^{-4/3}c_{10}\mathrm{I}_1\right)\mathbf{I}-2J^{-4/3}c_{10}\boldsymbol{C}\\&+\left[2D_1(J-1)-\frac{2}{3}c_{01}J^{-5/3}\mathrm{I}_1-\frac{4}{3}c_{10}J^{-7/3}\mathrm{I}_2\right]J\boldsymbol{C}^{-1}\end{aligned} \tag{12}$$

Cauchy stress $\boldsymbol{\sigma}=\frac{1}{J}\boldsymbol{F}\boldsymbol{T}\boldsymbol{F}^{\mathrm{T}}$ is obtained by Eq. (12) as

$$\begin{aligned}\boldsymbol{\sigma}^{\mathrm{h}}&=\left(2J^{-5/3}c_{01}+2J^{-7/3}c_{10}\mathrm{I}_1\right)\boldsymbol{B}-2J^{-7/3}c_{10}\boldsymbol{B}^2\\&+\left[2D_1(J-1)-\frac{2}{3}c_{01}J^{-5/3}\mathrm{I}_1-\frac{4}{3}c_{10}J^{-7/3}\mathrm{I}_2\right]\mathbf{I}\end{aligned} \tag{13}$$

where the left Cauchy-Green deformation tensor is $\boldsymbol{B}=\boldsymbol{F}\boldsymbol{F}^{\mathrm{T}}$. According to the Cayley-Hamilton theorem

$$\boldsymbol{B}^3-\mathrm{I}_1\boldsymbol{B}^2+\mathrm{I}_2\boldsymbol{B}-\mathrm{I}_3\mathbf{I}=\mathbf{0} \tag{14}$$

the Eq. (14) can be expressed as

$$\begin{aligned}\boldsymbol{\sigma}^{\mathrm{h}}&=2J^{-5/3}c_{01}\boldsymbol{B}+2J^{-7/3}c_{10}\left(\mathrm{I}_2\mathbf{I}-\mathrm{I}_3\boldsymbol{B}^{-1}\right)\\&+\left[2D_1(J-1)-\frac{2}{3}c_{01}J^{-5/3}\mathrm{I}_1-\frac{4}{3}c_{10}J^{-7/3}\mathrm{I}_2\right]\mathbf{I}\\&=2J^{-5/3}c_{01}\boldsymbol{B}-2J^{-7/3}c_{10}\mathrm{I}_3\boldsymbol{B}^{-1}\\&+\left[2D_1(J-1)-\frac{2}{3}c_{01}J^{-2/3}\mathrm{I}_1+\frac{2}{3}J^{-7/3}c_{10}\mathrm{I}_2\right]\mathbf{I}\end{aligned} \tag{15}$$

3.4. The compression viscoelastic equation for kerogen

This study focuses on the constitutive relation of kerogen exhibiting small deformation. According to the Boltzmann superposition principle, the viscoelastic stress-strain relationship of kerogen for an infinitesimal deformation can be written as [49, 50]

$$\boldsymbol{\sigma}^{\mathrm{v}}=\int_{-\infty}^{t}\mathbb{C}(t-\tau):\frac{\mathrm{d}\boldsymbol{\varepsilon}^{\mathrm{v}}}{\mathrm{d}\tau}\mathrm{d}\tau \tag{16}$$

where $\mathbb{C}$ is the fourth order tensor of the relaxation modulus (time-dependent), $\boldsymbol{\varepsilon}^{\mathrm{v}}$ is the viscoelastic Cauchy strain.

Assuming kerogen is an isotropic material, $\mathbb{C}$ is expressed as [49, 51, 52]

$$\mathbb{C}(t)=\left[\Lambda(t)\delta_{ik}\delta_{pq}+G(t)\left(\delta_{ip}\delta_{kq}+\delta_{iq}\delta_{kp}\right)\right]\boldsymbol{e}_i\otimes\boldsymbol{e}_k\otimes\boldsymbol{e}_p\otimes\boldsymbol{e}_q \tag{17}$$

where $\Lambda(t)\cdot G(t)$ are the time-dependent Lamé parameters. The relaxation modulus satisfies the minor symmetry and major symmetry. There are

$$\begin{cases}\boldsymbol{s}^{\mathrm{v}}=\boldsymbol{\varepsilon}^{\mathrm{v}}-\frac{1}{3}(\mathrm{tr}\boldsymbol{\varepsilon}^{\mathrm{v}})\mathbf{I}\\ K(t)=\Lambda(t)+\frac{2}{3}G(t)\\ e_{\mathrm{V}}=\varepsilon_{mm}^{\mathrm{v}}=\mathrm{tr}\boldsymbol{\varepsilon}^{\mathrm{v}}\end{cases} \tag{18}$$

where the $\boldsymbol{s}^{\mathrm{v}}$ is the deviatoric strain tensor, $K(t)$ is the time-dependent bulk modulus, and $e_{\mathrm{V}}$is the volume strain. From Eqs. (16), (17) and (18), we obtain the following

$$\boldsymbol{\sigma}^{\mathrm{v}}=\int_{-\infty}^{t}\Lambda(t-\tau)\dot{\varepsilon}_{mm}^{\mathrm{v}}\mathbf{I}+2G(t-\tau)\dot{\boldsymbol{\varepsilon}}^{\mathrm{v}}\mathrm{d}\tau \tag{19}$$

The substitution of the second formula in Eq. (18) into Eq. (19) yields

$$\begin{aligned}\boldsymbol{\sigma}^{\mathrm{v}}&=\int_{-\infty}^{t}\Lambda(t-\tau)\dot{e}_{\mathrm{V}}\mathbf{I}+2G(t-\tau)\left(\dot{\boldsymbol{s}}^{\mathrm{v}}+\frac{1}{3}\dot{e}_{\mathrm{V}}\mathbf{I}\right)\mathrm{d}\tau\\&=\int_{-\infty}^{t}\Lambda(t-\tau)\dot{e}_{\mathrm{V}}\mathbf{I}+\frac{2}{3}G(t-\tau)\dot{e}_{\mathrm{V}}\mathbf{I}+2G(t-\tau)\dot{\boldsymbol{s}}^{\mathrm{v}}\mathrm{d}\tau\\&=\int_{-\infty}^{t}\mathrm{K}(t-\tau)\dot{e}_{\mathrm{V}}\mathbf{I}+2G(t-\tau)\dot{\boldsymbol{s}}^{\mathrm{v}}\mathrm{d}\tau\end{aligned} \tag{20}$$

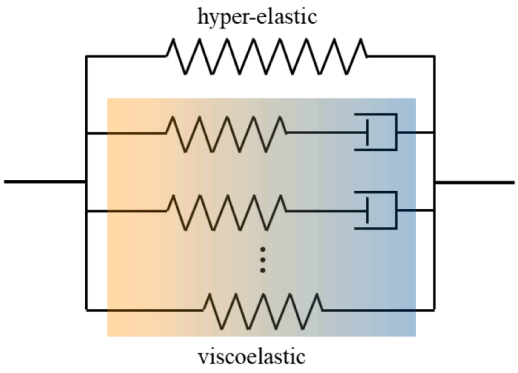

Fig. 7. The hyper-viscoelastic constitutive model of kerogen.

Via the given dimensionless Prony series

$$g(t) = g_\infty + \sum_{i=1}^{N} \mathrm{e}^{-\frac{t}{\theta_i}} \tag{21}$$

the bulk modulus $K(t)$ and shear modulus $G(t)$ for small deformation are generally expressed as [53]

$$\begin{cases} G(t) = G_0\left(g_\infty + \sum_{i=1}^{N} \mathrm{e}^{-\frac{t}{\theta_i}}\right) = G_\infty + \sum_{i=1}^{N} G_i \mathrm{e}^{-\frac{t}{\theta_i}} \\ K(t) = K_0\left(g_\infty + \sum_{i=1}^{N} \mathrm{e}^{-\frac{t}{\theta_i}}\right) = K_\infty + \sum_{i=1}^{N} K_i \mathrm{e}^{-\frac{t}{\theta_i}} \end{cases} \tag{22}$$

The stress can be written, by substituting Eq. (22) into Eq. (20), as follows

$$\begin{aligned} \boldsymbol{\sigma}^{\mathrm{v}} &= \int_{-\infty}^{t} \mathrm{K}(t-\tau)\dot{e}_{\mathrm{V}}\mathbf{I} + 2G(t-\tau)\dot{\boldsymbol{s}}^{\mathrm{v}}\mathrm{d}\tau \\ &= \int_{-\infty}^{t} \left(K_\infty + \sum_{i=1}^{N} K_i \mathrm{e}^{-\frac{t-\tau}{\theta_i}}\right)\dot{e}_{\mathrm{V}}\mathbf{I} + 2\left(G_\infty + \sum_{i=1}^{N} G_i \mathrm{e}^{-\frac{t-\tau}{\theta_i}}\right)\dot{\boldsymbol{s}}^{\mathrm{v}}\mathrm{d}\tau \\ &= \left(K_\infty e_{\mathrm{V}} + \sum_{i=1}^{N} K_i \int_{-\infty}^{t} \mathrm{e}^{-\frac{t-\tau}{\theta_i}}\dot{e}_{\mathrm{V}}\mathrm{d}\tau\right)\mathbf{I} + 2\left(G_\infty \boldsymbol{s}^{\mathrm{v}} + \sum_{i=1}^{N} G_i \int_{-\infty}^{t} \mathrm{e}^{-\frac{t-\tau}{\theta_i}}\dot{\boldsymbol{s}}^{\mathrm{v}}\mathrm{d}\tau\right) \end{aligned} \tag{23}$$

3.5. The hyper-viscoelastic model of kerogen under different strain rate

The scheme of hyper-viscoelastic model of kerogen is shown in Fig. 7. The relationships of the Cauchy stress and true strain of hyper-elastic and viscoelastic part are

$$\begin{cases} \boldsymbol{\sigma} = \boldsymbol{\sigma}^{\mathrm{v}} + \boldsymbol{\sigma}^{\mathrm{h}} \\ \boldsymbol{\varepsilon} = \boldsymbol{\varepsilon}^{\mathrm{v}} = \boldsymbol{\varepsilon}^{\mathrm{h}} \end{cases} \tag{24}$$

The total Cauchy stress is obtained by substituting Eqs. (15) and (23) into Eq. (24), which can be written as

$$\begin{aligned} \boldsymbol{\sigma} = &\left(K_\infty e_{\mathrm{V}} + \sum_{i=1}^{N} K_i \int_{-\infty}^{t} \mathrm{e}^{-\frac{t-\tau}{\theta_i}}\dot{e}_{\mathrm{V}}\mathrm{d}t\right)\mathbf{I} + 2\left(G_\infty \boldsymbol{s}^{\mathrm{v}} + \sum_{i=1}^{N} G_i \int_{-\infty}^{t} \mathrm{e}^{-\frac{t-\tau}{\theta_i}}\dot{\boldsymbol{s}}^{\mathrm{v}}\mathrm{d}t\right) \\ &+2J^{-5/3}c_{01}\boldsymbol{B} - 2J^{-7/3}\mathrm{I}_3\boldsymbol{B}^{-1} + \left[2D_1(J-1) - \frac{2}{3}c_{01}J^{-2/3}\mathrm{I}_1 + \frac{2}{3}J^{-7/3}c_{10}\mathrm{I}_2\right]\mathbf{I} \end{aligned} \tag{25}$$

In the principal stress direction, $\boldsymbol{B} = \sum_i \lambda_i^2 \boldsymbol{e}_i \otimes \boldsymbol{e}_i$, then the stress of hyper-elastic part is

Table 2
The parameters of the compressible hyper-viscoelastic model.

c_{01} (GPa)	c_{10} (GPa)	E_1 (GPa)	θ_1 (s)	E_∞ (GPa)
0.090	0.15	3.37	4.27×10^{-11}	1.09×10^{-9}

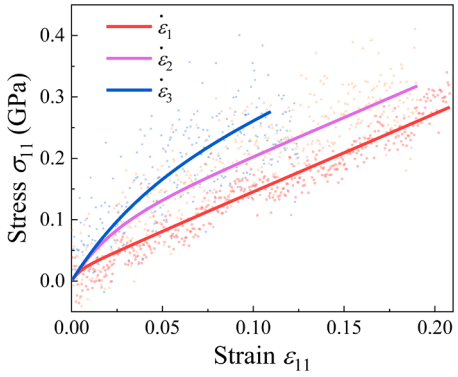

Fig. 8. The stress-strain curve of the compressible hyper-viscoelastic equation. The points are obtained by MD simulations, and the curves are obtained by fitting the points using the compressible hyper-elastic equation for kerogen.

$$\sigma_i^{\mathrm{h}} = 2J^{-5/3}c_{01}\lambda_i^2 - 2c_{10}J^{-7/3}\mathrm{I}_3\lambda_i^{-2} + 2D_1(J-1) - \frac{2}{3}c_{01}J^{-2/3}\mathrm{I}_1 + \frac{2}{3}J^{-7/3}c_{10}\mathrm{I}_2 \tag{26}$$

For the uniaxial extension $\sigma_{22} = \sigma_{33} = 0$, the function of stress, by elongation, can be expressed as

$$\sigma_{11}^{\mathrm{h}} - \sigma_{22}^{\mathrm{h}} = 2J^{-5/3}c_{01}\lambda_1^2 - 2J^{-1/3}c_{10}\lambda_1^{-2} - 2J^{-2/3}c_{01}\frac{1}{\lambda_1} + 2J^{-4/3}c_{10}\lambda_1 \tag{27}$$

For the viscoelastic part the stress can be written as

$$\begin{aligned} \sigma_{ii}^{\mathrm{v}} = &K_\infty e_{\mathrm{V}} + \sum_{i=1}^{N} K_i \int_{-\infty}^{t} \mathrm{e}^{-\frac{t-\tau}{\theta_i}}\dot{e}_{\mathrm{V}}\mathrm{d}\tau + 2G_\infty\left(\varepsilon_{ii} - \frac{e_{\mathrm{V}}}{3}\right) + 2 \\ &\times \sum_{i=1}^{N} G_i \int_{-\infty}^{t} \mathrm{e}^{-\frac{t-\tau}{\theta_i}}\left(\dot{\varepsilon}_{ii} - \frac{\dot{e}_{\mathrm{V}}}{3}\right)\mathrm{d}\tau \end{aligned} \tag{28}$$

When $\sigma_{22} = \sigma_{33} = 0$, the stress ($N = 1$) is

$$\sigma_{11}^{\mathrm{v}} - \sigma_{22}^{\mathrm{v}} = 2G_\infty(\varepsilon_{11} - \varepsilon_{22}) + 2G_1\int_{-\infty}^{t} \mathrm{e}^{-\frac{t-\tau}{\theta_1}}\left(\dot{\varepsilon}_{11} - \dot{\varepsilon}_{22}\right)\mathrm{d}\tau \tag{29}$$

Then the tensile stress is

$$\begin{aligned} \sigma_{11} &= \sigma_{11}^{\mathrm{v}} + \sigma_{11}^{\mathrm{h}} \\ &= 2J^{-5/3}c_{01}\lambda_1^2 - 2J^{-1/3}c_{10}\lambda_1^{-2} - 2J^{-2/3}c_{01}\frac{1}{\lambda_1} + 2J^{-4/3}c_{10}\lambda_1 \\ &\quad + E_\infty\varepsilon_{11} + E_1\int_{-\infty}^{t} \mathrm{e}^{-\frac{t-\tau}{\theta_1}}\dot{\varepsilon}_{11}\mathrm{d}\tau \end{aligned} \tag{30}$$

where $\lambda_1 = 1 + \varepsilon_{11}$, $J = \mathrm{d}v/\mathrm{d}V = \lambda_1\lambda_2\lambda_3$, $\varepsilon_{22} = -\nu\varepsilon_{11}$, and $G_1 = \frac{E_1}{2(1+\nu)}$.

According to the deformation of kerogen, the material is set as an isotropic material, and its Poisson's ratio ν is calculated at three strain rates, which is approximately 0.44. Thus, the Jacobian

$$J = \lambda_1\lambda_2\lambda_3 \approx (1+\varepsilon_{11})(1+\varepsilon_{22})(1+\varepsilon_{33}) = (1+\varepsilon_{11})(1-\nu\varepsilon_{11})^2 \tag{31}$$

The strain rate is considered as a constant within in the range of elastic deformation of kerogen. Then $t = \varepsilon/\dot{\varepsilon}$, and the Eq. (31) can be calculated as

$$\sigma_{11} = 2(1+\varepsilon_{11})^{-5/3}(1-0.44\varepsilon_{11})^{-10/3}\left[(1+\varepsilon_{11})^2-(1-0.44\varepsilon_{11})^2\right]$$
$$\cdot\left[c_{01}+c_{10}(1+\varepsilon_{11})^{-2/3}(1-0.44\varepsilon_{11})^{2/3}\right]+E_\infty\varepsilon_{11}+E_1\theta_1\dot{\varepsilon}_{11}\left(1-e^{-\frac{\varepsilon_{11}}{\dot{\varepsilon}_{11}\theta_1}}\right) \quad (32)$$

The mechanical behaviour of kerogen was performed by Eq. (32) under different strain rates. c_{01}, c_{10}, E_1, θ_1, and E_∞ are the material constants, which are obtained by global fitting of three groups of data. The parameters of constitutive equation of kerogen have been listed in Table 2. The calculating results are in good agreement with those of the simulations in Fig. 8. The model can reflect the material hardening phenomenon caused by the increase of the strain rate.

4. Conclusions

Based on the established molecular aggregate, the mechanical properties of kerogen are studied using Reaxff-MD. The dynamic response of kerogen from deformation to fracture is established under uniaxial tensile loads. The results show that the higher strain rate hardens kerogen. The elastic mechanical behaviour of kerogen is compressible and nonlinear. Furthermore, the ultimate strength increases with strain rate, while the fracture strain decreases.

The microscopic mechanism of intermolecular interactions of kerogen was obtained during stretching. In the plastic phase, the stress oscillation event occurs, and the micro-mechanism of which is related to the formation and breaking of H bonds. The H bond breaking brings partial stress release, then strain hardening occurs with some H bonds forming. Kerogen is easier to fracture at a higher strain rate. From the point of view of intermolecular interaction, the fracture of kerogen is mainly caused by the π-π interaction and H bonds broken.

A compressible hyper-viscoelastic constitutive model of kerogen is established, which accurately describes the mechanical behaviour of kerogen under different strain rates. The whole process of the mechanical response of kerogen deformation is obtained, which is hard to be obtained by experiments. The initial elastic moduli obtained by MD simulations are reasonable. Thus, the mechanical properties of kerogen obtained by Reaxff-MD are valuable for further research on the role of kerogen in reservoir mechanical behaviour.

CRediT authorship contribution statement

Xiaohe Wang: Methodology, Software, Formal analysis, Data curation, Writing - original draft, Visualization, Investigation, Writing - review & editing. **Xianfu Huang:** Formal analysis, Software, Writing - review & editing. **Mengni Gao:** Formal analysis, Validation, Writing - review & editing. **Ya-Pu Zhao:** Conceptualization, Methodology, Resources, Funding acquisition, Supervision, Project administration.

Declaration of Competing Interest

The authors declare that they have no known competing financial interests or personal relationships that could have appeared to influence the work reported in this paper.

Acknowledgements

This work was supported by the National Natural Science Foundation of China (NSFC, Grants 12032019, 11872363, 51861145314); the Chinese Academy of Sciences (CAS) Key Research Program of Frontier Sciences (Grant QYZDJ-SSW-JSC019), and the CAS Strategic Priority Research Program (Grant XDB22040401).

References

[1] Shen W, Zhao Y-P. Combined effect of pressure and shear stress on penny-shaped fluid-driven cracks. J Appl Mech-Trans ASME 2018;85.
[2] Shen W, Zhao Y-P. Quasi-static crack growth under symmetrical loads in hydraulic fracturing. J Appl Mech-Trans ASME 2017;84.
[3] Shen W, Yang F, Zhao Y-P. Unstable crack growth in hydraulic fracturing: the combined effects of pressure and shear stress for a power-law fluid. Eng Fract Mech 2020;225:106245.
[4] Sun F, Shen W, Zhao Y-P. Deflected trajectory of a single fluid-driven crack under anisotropic in-situ stress. Extreme Mech Lett 2019;29:100483.
[5] Wu T, Firoozabadi A. Mechanical properties and failure envelope of kerogen matrix by molecular dynamics simulations. J Mater Chem C 2020;124:2289–94.
[6] Bobko C, Ulm F-J. The nano-mechanical morphology of shale. Mech Mater 2008; 40:318–37.
[7] Lankford Jr J. Dynamic strength of oil shale. Society of Petroleum Engineers Journal 1976;16:17–22.
[8] Shi X, He Z, Long S, Peng Y, Li D, Jiang S. Loading rate effect on the mechanical behavior of brittle longmaxi shale in nanoindentation. Int J Hydrogen Energy 2019;44:6481–90.
[9] Wilkinson TM, Zargari S, Prasad M, Packard CE. Optimizing nano-dynamic mechanical analysis for high-resolution, elastic modulus mapping in organic-rich shales. J Mater Sci 2015;50:1041–9.
[10] Zeszotarski JC, Chromik RR, Vinci RP, Messmer MC, Michels R, Larsen JW. Imaging and mechanical property measurements of kerogen via nanoindentation. Geochim Cosmochim Acta 2004;68:4113–9.
[11] Eliyahu M, Emmanuel S, Day-Stirrat RJ, Macaulay CI. Mechanical properties of organic matter in shales mapped at the nanometer scale. Mar Petrol Geol 2015;59: 294–304.
[12] Zargari S, Wilkinson TM, Packard CE, Prasad M. Effect of thermal maturity on elastic properties of kerogen. Geophysics 2016;81:M1–6.
[13] Zargari S, Prasad M, Mba KC, Mattson ED. Organic maturity, elastic properties, and textural characteristics of self resourcing reservoirs. Geophysics 2013;78: D223–DD35.
[14] Javadpour F, Moravvej Farshi M, Amrein M. Atomic-force microscopy: a new tool for gas-shale characterization. J Can Pet Technol 2012;51:236–43.
[15] Emmanuel S, Eliyahu M, Day-Stirrat RJ, Hofmann R, Macaulay CI. Impact of thermal maturation on nano-scale elastic properties of organic matter in shales. Mar Petrol Geol 2016;70:175–84.
[16] Eichmann S, Jacobi D, Haque M, Burnham N. Non-destructive investigations of the thermal maturity and mechanical properties of source rocks. J Petrol Geol 2018;41: 421–46.
[17] Kabir P, Ulm F-J, Akono A-T. Rate-independent fracture toughness of gray and black kerogen-rich shales. Acta Geotech 2017;12:1207–27.
[18] Huang X, Zhao Y-P. Characterization of pore structure, gas adsorption, and spontaneous imbibition in shale gas reservoirs. J Petrol Sci Eng 2017;159:197–204.
[19] Khatibi S, Aghajanpour A, Ostadhassan M, Ghanbari E, Amirian E, Mohammed R. In: SPE Canada unconventional resources conference. society of petroleum engineers; 2018.
[20] Han Y, Al-Muntasheri G, Katherine LH, Abousleiman YN. In: Tensile mechanical behavior of kerogen and its potential implication to fracture opening in kerogen-rich shales (KRS). 50th US rock mechanics/geomechanics symposium. American Rock Mechanics Association; 2016.
[21] Thomas JJ, Valenza II JJ, PR Craddock, KD Bake, AE Pomerantz. The neutron scattering length density of kerogen and coal as determined by CH3OH/CD3OH exchange. Fuel 2014;117:801–8.
[22] Gu X, Cole DR, Rother G, Mildner DF, Brantley SL. Pores in Marcellus shale: a neutron scattering and FIB-SEM study. Energy Fuels 2015;29:1295–308.
[23] Kang D, Wang X, Zheng X, Zhao Y-P. Predicting the components and types of kerogen in shale by combining machine learning with NMR spectra. Fuel 2021; 290:120006.
[24] Bousige C, Ghimbeu CM, Vix-Guterl C, Pomerantz AE, Suleimenova A, Vaughan G, et al. Realistic molecular model of kerogen's nanostructure. Nat Mater 2016;15: 576–82.
[25] Wang X, Zhao Y-P. The time-temperature-maturity relationship: a chemical kinetic model of kerogen evolution based on a developed molecule-maturity index. Fuel 2020;278:118264.
[26] Huang X, Zhao Y-P, Wang X, Pan L. Adsorption-induced pore blocking and its mechanisms in nanoporous shale due to interactions with supercritical CO2. J Petrol Sci Eng 2019;178:74–81.
[27] Yu H, Xu H, Fan J, Zhu YB, Wang F, Wu H. Transport of shale gas in microporous/ nanoporous media: molecular to pore-scale simulations. Energy Fuels 2020.
[28] Berthonneau J, Obliger A, Valdenaire P-L, Grauby O, Ferry D, Chaudanson D, et al. Mesoscale structure, mechanics, and transport properties of source rocks' organic pore networks. Proc Natl Acad Sci 2018;115:12365–70.
[29] Odegard GM, Jensen BD, Gowtham S, Wu J, He J, Zhang Z. Predicting mechanical response of crosslinked epoxy using ReaxFF. Chem Phys Lett 2014;591:175–8.
[30] Liu L, Jaramillo-Botero A, Goddard III WA, Sun H. Development of a ReaxFF reactive force field for ettringite and study of its mechanical failure modes from reactive dynamics simulations. J Phys Chem A 2012;116:3918–25.
[31] Cranford SW, Buehler MJ. Mechanical properties of graphyne. Carbon 2011;49: 4111–21.
[32] Jensen BD, Wise KE, Odegard GM. The effect of time step, thermostat, and strain rate on ReaxFF simulations of mechanical failure in diamond, graphene, and carbon nanotube. J Comput Chem 2015;36:1587–96.

[33] Shin YK, Kwak H, Zou C, Vasenkov AV, van Duin AC. Development and validation of a ReaxFF reactive force field for Fe/Al/Ni alloys: molecular dynamics study of elastic constants, diffusion, and segregation. J Phys Chem A 2012;116:12163–74.
[34] Vashisth A, Ashraf C, Bakis CE, van Duin AC. Effect of chemical structure on thermo-mechanical properties of epoxy polymers: comparison of accelerated ReaxFF simulations and experiments. Polymer 2018;158:354–63.
[35] Sindt O, Perez J, Gerard J. Molecular architecture-mechanical behaviour relationships in epoxy networks. Polymer 1996;37:2989–97.
[36] Wu X, Moon RJ, Martini A. Crystalline cellulose elastic modulus predicted by atomistic models of uniform deformation and nanoscale indentation. Cellulose 2013;20:43–55.
[37] Ungerer P, Collell J, Yiannourakou M. Molecular modeling of the volumetric and thermodynamic properties of kerogen: influence of organic type and maturity. Energy & Fuels 2015;29:91–105.
[38] Tong J, Jiang X, Han X, Wang X. Evaluation of the macromolecular structure of Huadian oil shale kerogen using molecular modeling. Fuel 2016;181:330–9.
[39] Wang X, Huang X, Lin K, Zhao Y-P. The constructions and pyrolysis of 3D kerogen macromolecular models: experiments and simulations. Glob Chall 2019;3:1900006.
[40] Qin KZ, Wang R, Jia S. Chemical structure investigation of Maoming oil shale kerogen by supercritical gas extraction. Energ source 1984;7:237–55.
[41] Zong QK. A method of measuring molecular weight of kerogen. Petrol Geol Exp 1984;11.
[42] Okiongbo KS, Aplin AC, Larter SR. Changes in type II Kerogen density as a function of maturity: evidence from the kimmeridge clay formation. Energy Fuels 2005;19:2495–9.
[43] Liu L, Liu Y, Zybin SV, Sun H, Goddard III WA. ReaxFF-lg: correction of the ReaxFF reactive force field for London dispersion, with applications to the equations of state for energetic materials. J Phys Chem A 2011;115:11016–22.
[44] Zhao Y-P. Modern continuum mechanics. 1st ed. Beijing, China: Science Press; 2016.
[45] Bracq A, Haugou G, Bourel B, Maréchal C, Lauro F, Roth S, et al. On the modeling of a visco-hyperelastic polymer gel under blunt ballistic impacts. Int J Impact Eng 2018;118:78–90.
[46] Pouriayevali H, Guo Y, Shim V. A constitutive description of elastomer behaviour at high strain rates–A strain-dependent relaxation time approach. Int J Impact Eng 2012;47:71–8.
[47] Yang L, Shim V, Lim C. A visco-hyperelastic approach to modelling the constitutive behaviour of rubber. Int J Impact Eng 2000;24:545–60.
[48] Zhao Y-P. A course in rational mechanics. 1st ed. Beijing, China: Science Press; 2020.
[49] Cho KS. Viscoelasticity of polymers. 1st ed. New York, USA: Springer; 2016.
[50] Gong C., Chen Y., Li T., Liu Z., Zhuang Z., Guo B., et al. Free volume based nonlinear viscoelastic model for polyurea over a wide range of strain rates and temperatures. Mech Mater 152:103650.
[51] Sadeghpour E, Guo Y, Chua D, Shim VP. Dynamic stress–strain response of graphene nanocomposites. Int J Impact Eng 2020;145:103690.
[52] Wang LL, Yu T-X, Li YC. Progress in impact dynamics. 1st ed. He Fei, China: Press of China University of Science and Technology; 1992.
[53] Ghorbanoghli A, Narooei K. A new hyper-viscoelastic model for investigating rate dependent mechanical behavior of dual cross link self-healing hydrogel. Int J Mech Sci 2019;159:278–86.